



0191-8141(94)00081-6

Development of highly non-cylindrical folds around rigid ellipsoidal inclusions in bulk simple shear regimes: natural examples and experimental modelling

F. G. MARQUES* and P. R. COBBOLD†

*Department of Geologia, Fac. Ciências, University of Lisboa, Edifício C2, Piso 5, 1700 Lisboa, Portugal

†Centre Armoricaïn d'Etude Structurale des Socles (CNRS—Université de Rennes) Campus de Beaulieu, 35042 Rennes-Cedex, France

(Received 1 November 1993; accepted in revised form 5 July 1994)

Abstract—The three-dimensional development of strongly non-cylindrical folds around competent ellipsoidal inclusions in bulk simple shear regimes is studied in experiments and natural examples. Examples from the Continental Allochthonous Terrane of the Bragança Nappe Complex (NE Portugal) show rim folds and sheath folds associated with different parts of rigid ellipsoidal boudins. Experimental work has been carried out with models made from analogue materials (silicone putty and plasticine) and deformed in a simple shear machine. We have considered three different models to simulate natural examples, and the results show that fold morphology depends on the shape of the inclusion and position around the inclusion. Although the bulk deformation regime is layer parallel homogeneous simple shear, we can distinguish local deformation regimes responsible for the folding associated with different parts of the rigid body. Flow and strain patterns must therefore be complex around inclusions or populations of inclusions. Prolate to oblate strain ellipsoids can be expected in different positions close to the rigid inclusion. In our experiments, the competent inclusions do not rotate synthetically with the applied bulk simple shear (e.g. clockwise rotation of inclusion in dextral shear). Instead, they back-rotate, early in the shearing history, and keep this position throughout the experiment. This is the result of the size relationship between the inclusion and the finite width of the shear zone. The fold pattern around rigid inclusions may be used as a shear sense criterion.

INTRODUCTION

Many originally high-grade metamorphic terranes exhibit retrogression into amphibolite or even greenschist facies. Examples include the Continental Allochthonous Terrane of the Bragança and Morais Massifs, NE Portugal; upper allochthon of the Cabo Ortegal and Ordenes Massifs, NW Spain; Leptino-amphibolitic Group of the French Massif Central; high-pressure terrane of Ile de Groix, France. Immersed in the foliated retrogressed rock, competent boudins can be found that usually preserve the high-grade metamorphic mineral parageneses and textures. In such terranes, folds are commonly seen around the competent boudins.

Our experimental study was based on the natural examples observed in the Bragança CAT, described in detail elsewhere (Marques 1989, Marques *et al.* 1992, Marques 1993). In this nappe, two main types of granulites have been distinguished: (1) granulites whose mineral parageneses and mineral inclusions in garnets record a complex clockwise *PTt* path with early HP/HT granulite facies, and later variable recrystallization in amphibolite facies conditions during blastomylonitization (Munhá & Marques 1987); (2) coronitic gabbros that intruded the granulites of (1) and that record a much simpler *PTt* path of extensive isobaric cooling (Munhá & Marques 1988). During blastomylonitization, both types of granulites have been strongly deformed and rigid ellipsoidal boudins have formed by a mechanism of ductile boudinage of the more competent layers. The

final result is a blastomylonitic amphibolite whose flat-lying foliation is strongly folded around rigid ellipsoidal boudins of variable size. These generally preserve high-grade metamorphic or igneous mineral parageneses and textures, showing that they have behaved competently during deformation. Most fold hinges are parallel to a prominent mineral stretching lineation; cross-sections show typical elliptical traces of sheath folds (Fig. 3a) and are not associated with boudins. However, decimetric boudins, or greater, always show associated folds. In general, we have observed sections (usually not favourably oriented) of boudins and associated folds, but in a few critical outcrops we have been able to observe patterns of folds cropping out around rigid ellipsoidal boudins (Figs. 1, 2, 3b and 4c). From these partial patterns, Marques (1989) and Marques (1993) proposed a complete pattern of folds developed in association with rigid boudins (Fig. 6). All structures present in the Bragança CAT appear typical of non-coaxial deformation, and have led to the conclusion that the main deformation regime must have been bulk layer parallel simple shear.

Experimental and theoretical investigations of the motion of rigid ellipsoidal particles embedded in a viscous matrix have been performed since early this century (e.g. Jeffery 1922, Taylor 1923, Mason & Manley 1957, Bretherton 1962, Gay 1968, Cox 1971, Reed & Tryggvason 1974, Ferguson 1979, Harris *et al.* 1979, Hinch & Leal 1979, Freeman 1985). More recently, many sets of experiments have determined the rotation,

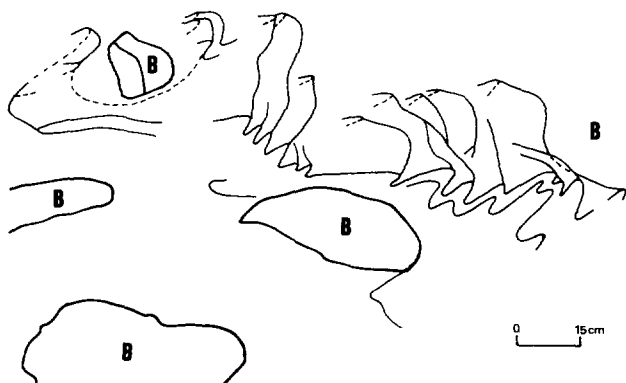


Fig. 1. Sketch from detailed photograph of the left tail of the boudin of Fig. 4(c). Smaller boudins (B) with associated folds jam at the upper-rear part of the larger boudin. Folds almost completely surround the boudin on the upper left corner of the image at its equatorial region.

and deformation patterns for rigid or deformable inclusions immersed in a viscous medium (e.g. Ghosh & Sengupta 1973, Ghosh 1975, Ghosh & Ramberg 1976, Passchier & Simpson 1986, Van den Driessche 1986, Van den Driessche & Brun 1987, Ildefonse *et al.* 1992, Ildefonse & Mancktelow 1993, Passchier & Sokoutis 1993).

Experimental work on the development of strongly non-cylindrical folds with sheath-like shape has also been carried out (e.g. Cobbold & Quinquis 1980, Ghosh & Sengupta 1984, Brun & Merle 1988). Cobbold & Quinquis (1980) showed that, in bulk simple shear regimes, sheath folds may develop passively from pre-existing non-cylindrical deflections of the layering (models 1 and

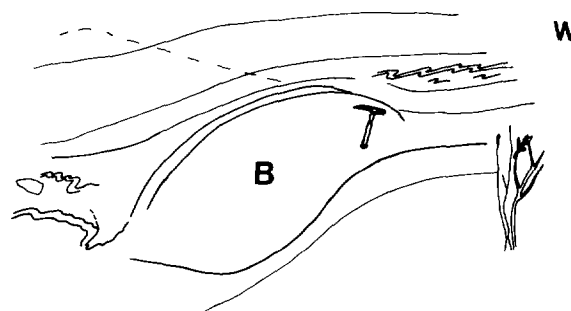


Fig. 2. Sketch from photograph of Fig. 4(c) for a better visualization of the position and geometry of folds around a rigid boudin (B).

2). They also obtained non-cylindrical folds during boudinage of competent layers in bulk simple shear (model 3). Skjerna (1989) showed that tubular folds may develop by the superposition of layer-parallel bulk simple shear on transverse non-cylindrical folds (i.e. with hinges at a small angle to the shear direction).

Previous experimental work, to our knowledge, has not dealt with the development of non-cylindrical folds around competent ellipsoidal bodies immersed in a ductile matrix. Knowing the fold pattern around rigid boudins in natural ductile shear zones, the theoretical relationship of rigid boudin/ductile matrix and a most probable deformation regime (simple shear), we have tried to reproduce the observed natural structures in laboratory. The experiments now presented show the complete fold pattern that can develop around rigid inclusions during bulk homogeneous simple shear.

The experimental work has been carried out with

Captions to figures on following pages

Fig. 3. (a) Natural example of sheath folds from Bragança (near map coordinates M-299.875, P-533.525). Section normal to long axes of sheaths developed in blastomylonitic granulite. Notice elliptical and mushroom-like traces. (b) Sheath fold associated with the upper rear of a prolate boudin (B), (near map coordinate M-300.050, P-536.175). It is possible that another boudin has existed on the eroded part of the outcrop (towards the observer) and that the sheath fold has developed between the two boudins as illustrated in Fig. 9. The pencil lies on top of the sheath fold and is parallel to the stretching lineation. The rock is an alternating succession of metaperidotite, hornblendite and metapyroxenite. On the image we can see other folds around the boudin. Top to the left sense of shear. (c) Photomicrograph of a σ porphyroclast system in kyanite-garnet-gneiss (map coordinates near M-302.000, P-539.675). The central porphyroclast dips to the right, opposite to the top sense of shear. Note the presence of shear bands above and below the porphyroclast, defined by the concentration of finely recrystallized mica (darker traces on the image, marked by arrows). Top to the left sense of shear (also deduced from δ porphyroclasts and mica-fish present in the same sample). 18 \times .

Fig. 4. (a) Outcrop photograph of cross-section of sheath fold associated with a boudin (B) of flaser gabbro, from near map coordinate M-300.700, P-537.625. Note that the sheath is very flattened because the boudin has a very large curvature ratio. Compare this natural example with the experimental result in (b). Top to the observer sense of shear. Hammer for scale. (b) Photograph of cross-section of experimental result with an oblate rigid inclusion. Section very close to the rigid inclusion. Compare with natural example in (a). Top to the observer sense of shear. (c) Granulitic boudin (B) inside flat-lying ductile shear zone filled with carbonates, map coordinates near M-297.925, P-539.600. Arrows indicate sites of preferential development of folds. The boudin exhibits a geometry typical of σ tailed porphyroclasts and is tilted opposite to the top sense of shear. A similar tilting and distribution of folds around rigid inclusions was observed during the experiments. All structures indicate top to the right sense of shear. Hammer for scale. (d) Longitudinal section (parallel to shear direction) of the model drawn in Fig. 8. In this picture we can see the complete pattern of folds around the rigid inclusion. Notice that the equatorial plane of the rigid inclusion dips to the left, although shear sense is top to the right.

Fig. 5. (a)–(c) Oblate rigid inclusion embedded in transparent silicone. (a) Lateral view (longitudinal section) of early stage of deformation. Note that the rigid inclusion is already dipping to the right, opposite to the top sense of shear. Top to the left sense of shear. (b) Same experiment as in (a), seen from the opposite side of the simple shear machine, at the final stage of deformation. (c) Top view of the model, through the upper transparent silicone layer, after deformation with a shear strain value close to 3 (top of the model moved to the right during shear). A passive grid was marked on top of the upper brown silicone layer. Note that the shape of the fold is not tubular as in (d), and that the hinge span (measured along Y) is identical to the width of the inclusion, and much wider than the sheath from model (d). The ellipse long axes near the sides of the inclusion show that there was dextral transcurrent movement at the left (L) side, and sinistral at the right side (R). The ellipses close to the confining side walls do not show drag and the grid at the front of the inclusion shows practically no deformation. (d) Prolate rigid inclusion (model 3). Top view of the model, through the upper transparent silicone layer, after deformation with a shear strain value close to 3 (top of the model moved to the right during shear). Note the tubular shape of the sheath fold developed at the upper front and the hinge span (measured along Y) equal to the width of the inclusion. A rim syncline formed at the upper rear and the two bumps at each side of the base of the tubular fold correspond to the rim anticline developed at the lower front. The small amplitude folds contouring the upper rear part of the inclusion do not show drag on the side walls confining the model.

Non-cylindrical folds around inclusions in simple shear

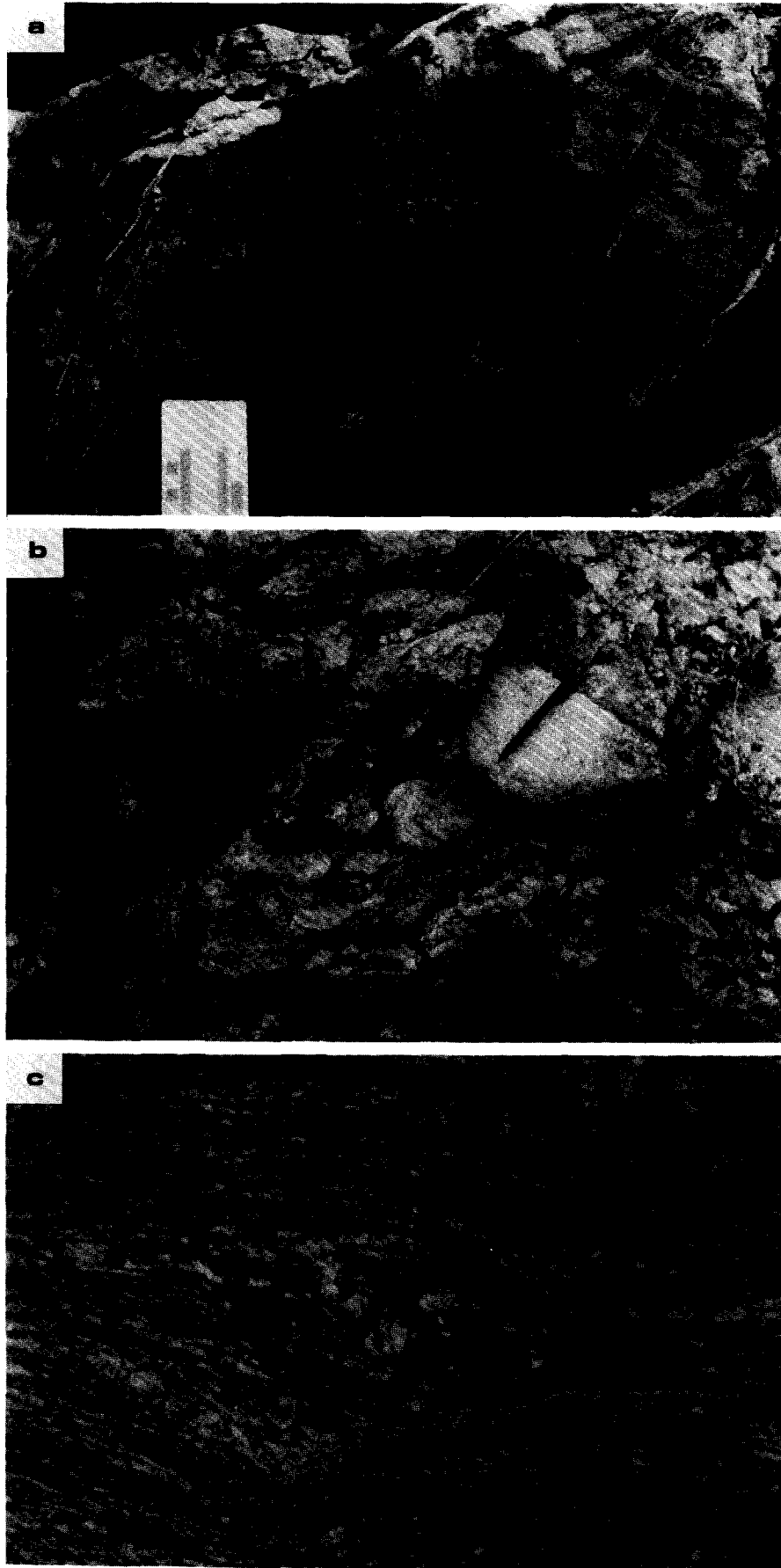


Fig. 3.

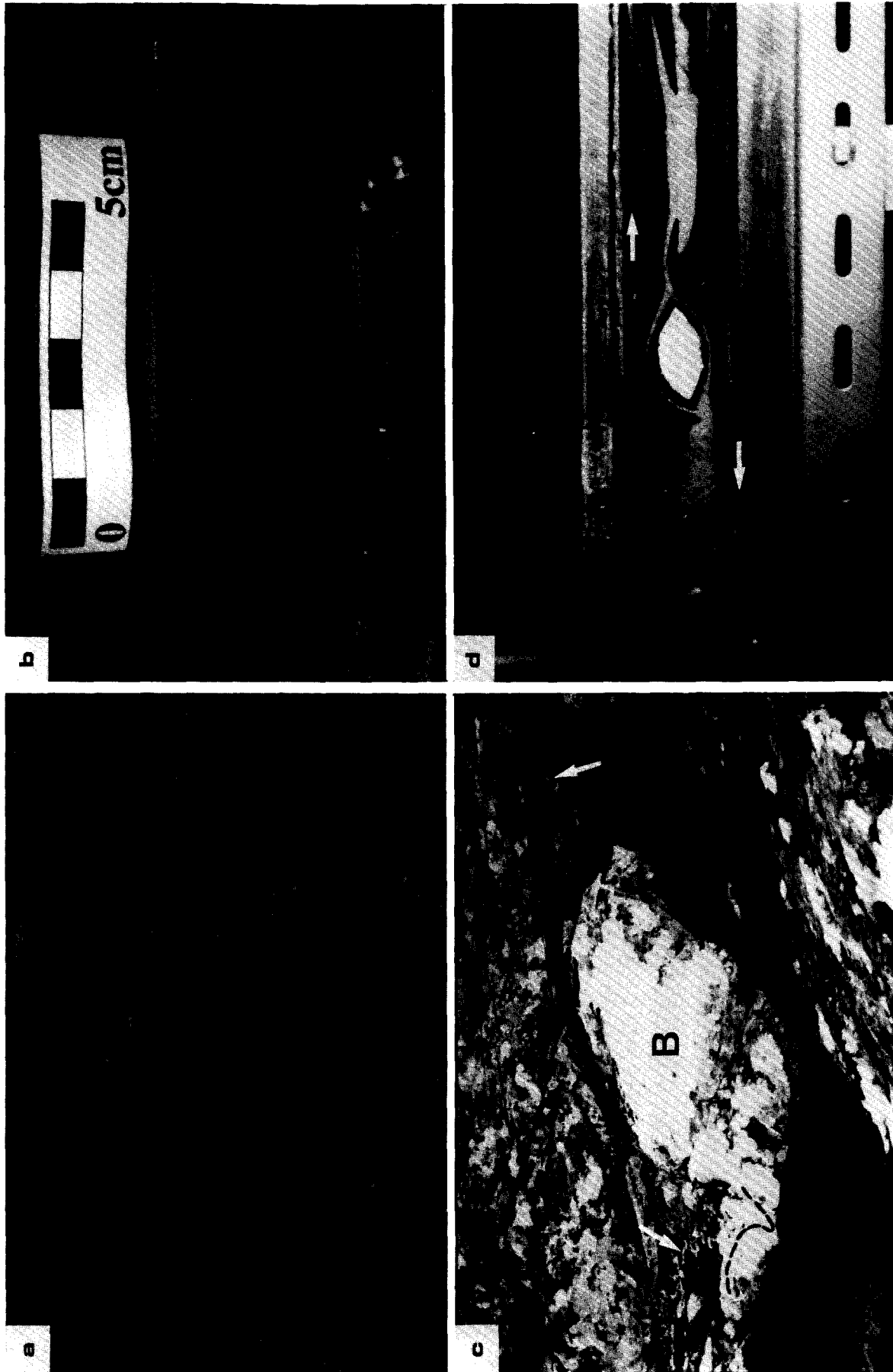


Fig. 4.

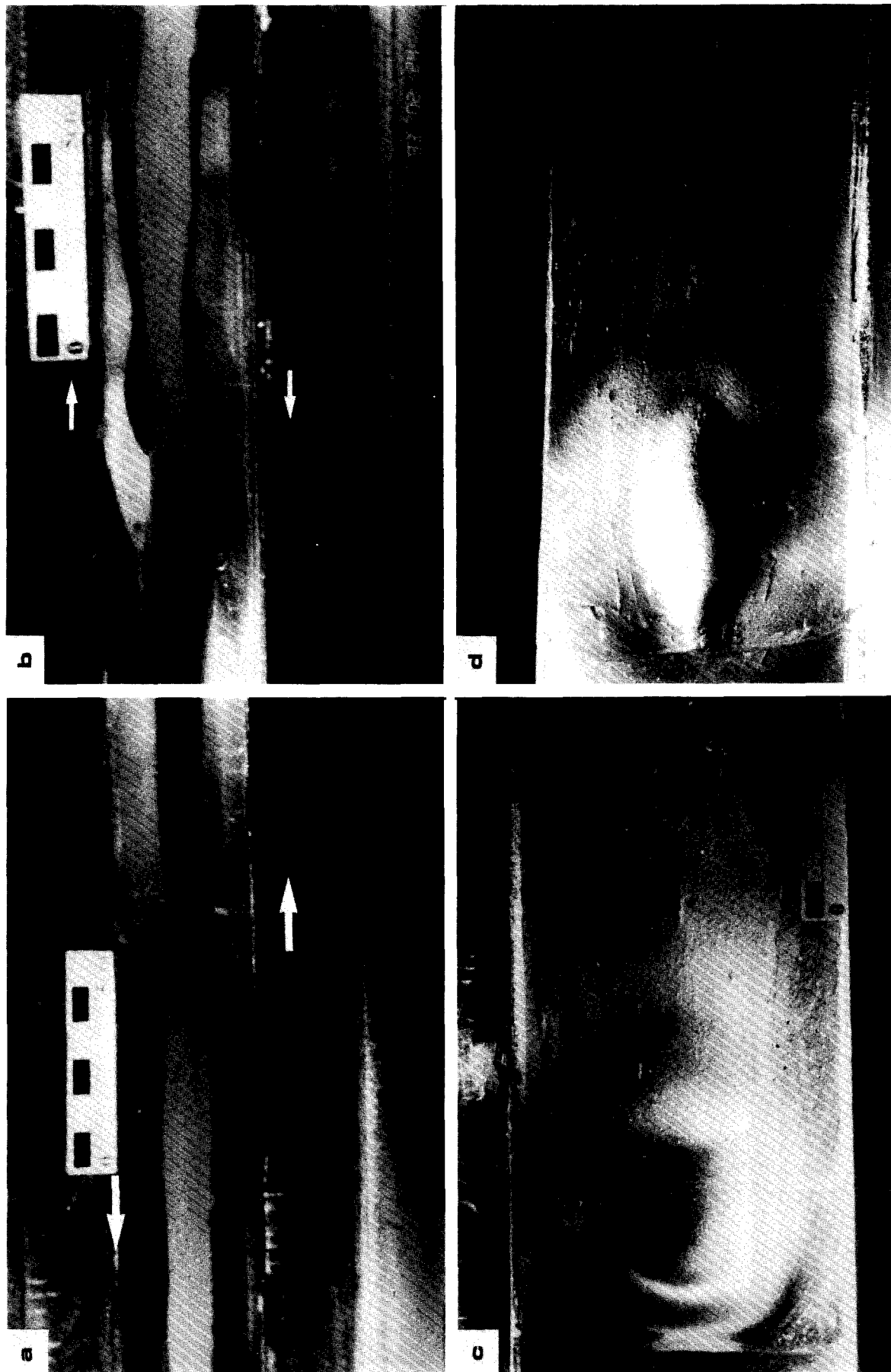


Fig. 5.

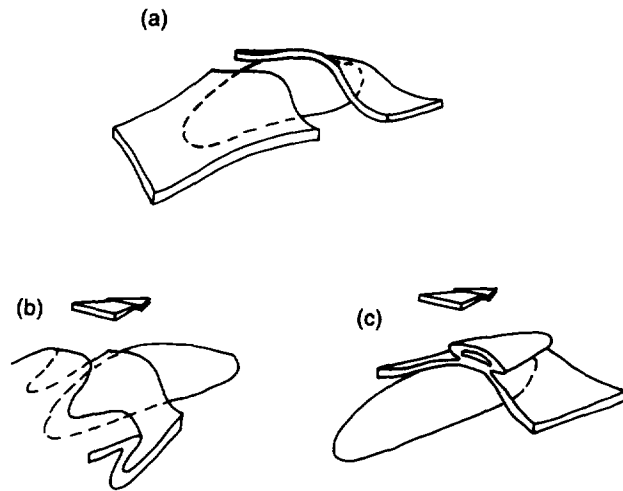


Fig. 6. Interpretative sketch drawn from partial observations of natural folds associated with rigid boudins. From Marques (1989) and Marques (1993).

models using the following analogue materials. Silicone putty (Rhodorsil gomme speciale 70009 manufactured by Rhone-Poulenc, France) was used to simulate the ductile matrix. Plasticine (standard violet plasticine manufactured by Harbutt's Plasticine Ltd, Bathampton, Bath, England) was used to simulate the rigid boudin. In two experiments, for a better visualization of the three-dimensional development of the folds around the inclusions, we used, a transparent matrix of polydimethylsiloxane manufactured by Dow Corning of Great Britain under the trade name SGM 36 (Weijermars 1986a, b, c). Although this transparent silicone present a more elastic behaviour, at the applied strain rates the final results are quite similar to the ones obtained with the pink silicone. All models have been deformed in a simple shear machine, the same one used and described by Cobbold & Quinquis (1980).

FOLDING AROUND RIGID ELLIPSOIDAL INCLUSIONS

By definition, in homogeneous simple shear, folds do not develop passively from planar surfaces at any angle

to the shear plane or direction. Thus, if folds are expected to develop passively in bulk homogenous simple shear regimes, then non-planar surfaces must be subjected to deformation. Moreover, if sheath folds are expected to develop, then homogeneous simple shear must affect non-cylindrical surfaces. On the other hand, if we insert ellipsoidal rigid bodies (which have non-cylindrical surfaces) in the model, then local variations in the deformation regime will occur, which could lead to the development of highly non-cylindrical folds of different shapes: the subject of our experimental investigation.

According to Donath & Parker (1964), passive folding can occur during homogeneous deformation of layers with identical rheological properties. When layers present contrasting rheology, deformation may be locally heterogeneous and unstable, and layers may undergo active folding. If we take this definition strictly, then the folds associated with rigid inclusions developed passively during our experiments, because layering is made up of coloured silicone layers with identical rheological properties. Cobbold & Quinquis (1980) also considered the folding to be passive in their models 2 and 3 which included resistant plasticine layers.

For a better understanding, and because differences exist around the inclusion, we have considered the rigid inclusion divided in four quadrants: upper and lower front (and frontal tail), and upper and lower rear (and rear tail) (Fig. 7b). This division is only valid for sub-horizontal shear zones as observed in Bragança.

The plasticine we used had a density close to 1.9 g cm^{-3} and silicone a density close to 1.2 g cm^{-3} ; hence the necessity to carve a polystyrene core to lower the density of the plasticine inclusion to values close to 1.2 g cm^{-3} .

In the reconstruction of the deformed models, besides the serial sections normal to the shear direction (cross-sections), we have also performed several sections parallel to the shear direction (longitudinal sections) for a better interpolation of the structures from one cross-section to the next. The coordinate system is used of x, y, z for the inclusion, and X, Y, Z for the matrix, with XY

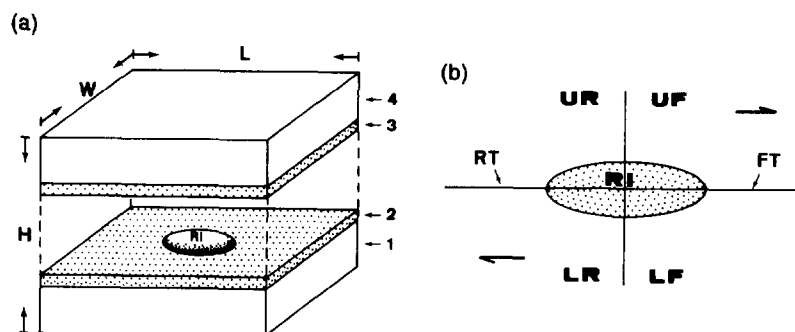


Fig. 7. (a) Design of the model for all experiments. Model dimensions are $L = 400 \text{ mm}$, $W = 100 \text{ mm}$ and $H = 50 \text{ mm}$. (1) Lower pink silicone layer (20 mm thick). (2) Lower brown silicone half-layer (5 mm thick). The prolate or oblate plasticine inclusions (RI) were put on top of this layer and left to settle by their own weight. In some of the experiments we have put a very thin film of lubricant (neutral liquid soap) between layers 2 and 3 and around the inclusion. (3) Upper brown silicone half-layer (5 mm thick). (4) Upper pink silicone layer (20 mm thick). In two experiments we used transparent silicone instead of pink silicone. (b) Sketch to illustrate the proposed sub-division of a rigid inclusion (RI) within a sub-horizontal ductile shear zone. Structures developed at the upper front (UF) are identical to the ones formed at the lower rear (LR). The same is true for the structures developed at the upper rear (UR) and lower front (LF). FT—frontal tail. RT—rear tail. Arrows indicate sense of shear.

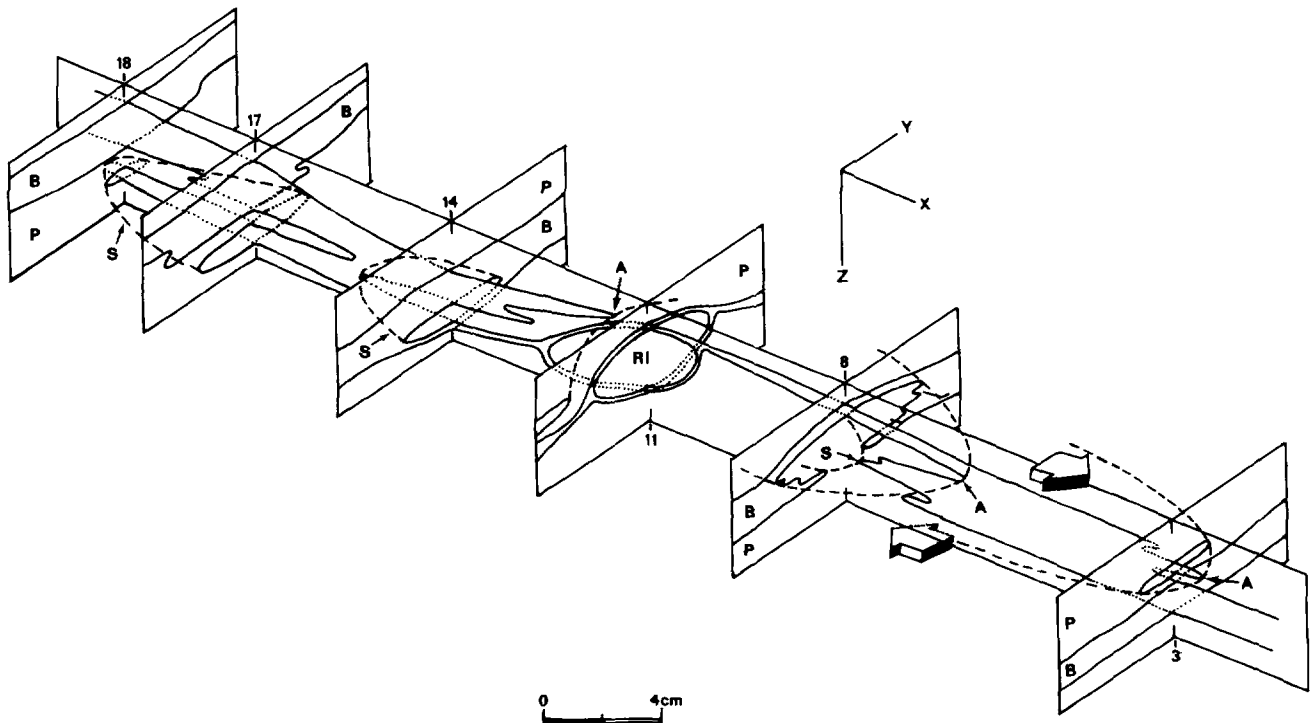


Fig. 8. Detail of model 2 (oblate rigid inclusion) shown in Fig. 4(d): experimental result (shear strain = 7). Block diagram of the layered silicone model was constructed from serial cross-sections (normal to the shear direction) and from longitudinal sections (parallel to the shear direction). Only the rigid inclusion (RI) and brown silicone half-layers are represented, and only six cross-sections are shown for clarity. B—brown silicone; P—pink silicone; A—antiform (anticline); S—synform (syncline).

the 'shear plane' and Y the direction of no strain for bulk simple shear.

Three models are presented, depending on the shape and number of the rigid inclusions. In model 1 we have used a prolate inclusion, in model 2 an oblate inclusion and in model 3 two prolate inclusions. These models have all been built with similar geometries as illustrated in Fig. 7(a). In all models two variants have been used: (1) a 'dry' model in which the several silicone layers have been put on top of one another without any intervening liquids; (2) a model in which we have used a very thin film of lubricant (neutral liquid soap) between the two brown silicone half-layers and around the rigid inclusion.

Model 1—prolate rigid inclusion

The prolate plasticine inclusion was moulded with principal dimensions $x = 85$ mm and $y = z = 25$ mm, and put on the middle of the top of the lower brown silicone half-layer with the longest axis coincident with the shear direction. The entire model was subjected to bulk homogeneous simple shear deformation with values of strain rate of about $6.6 \times 10^{-3} \text{ s}^{-1}$ and shear strain close to 7. Two types of folds can be distinguished associated with different parts of the inclusion: (1) two typical tubular folds developed at the upper front (anticline) and lower rear (syncline), and (2) two sets of rim synclines and anticlines developed at the upper rear and lower front. The experimental rim anticline/syncline formed at the upper rear of the rigid inclusion (Figs. 4d and 5d) is similar to the rim anticline/syncline associated with the

upper rear of rigid ellipsoidal boudins in the natural ductile shear zone of Fig. 1.

Model 2—oblate rigid inclusion

The oblate plasticine inclusion was moulded with principal dimensions $x = y = 60$ mm and $z = 27$ mm, and placed on the middle of the top of the lower brown silicone half-layer with the x/y plane parallel to the shear plane (and silicone layering). The model was subjected to bulk homogeneous simple shear with values of shear strain close to 7 and strain rate about $6.6 \times 10^{-3} \text{ s}^{-1}$. The reconstruction of the deformed model is illustrated in Fig. 8. The structures are comparable to model 1, but, as theoretically expected, the shape of the sheath folds is clearly different (compare Figs. 5c with d). With identical values of shear strain, the sheath folds in model 2 are much broader (greater span, measured along Y) and not typically tubular as in model 1. The experimental rim synclines/anticlines, as for model 1, are quite similar to those observed in natural examples (compare Figs. 4d and 5c with Fig. 1). The experimental upper frontal (Fig. 4b) and lower rear sheath folds are also very similar to the observed natural examples (Fig. 4, compare a and b).

As mentioned earlier, one of the experiments with an oblate inclusion was constructed with transparent silicone (Figs. 5a, b & c) instead of pink opaque silicone. In this model we printed a grid of squares with enclosed circles on top of the upper brown silicone half-layer, except in the region of the inclusion, because (1) the surface of the inclusion is not cylindrical (the orthogonal

grid was printed on a sheet of paper), and (2) the brown silicone immediately begins to flow sideways from the top of the inclusion, so the grid is no more rectangular. After deformation (Fig. 5c), several main features are immediately obvious. (1) Circles between the confining sidewalls and the inclusion have been transformed into strain ellipses with the long (λ_1) axis at a certain angle to the shear direction (implying transcurrent movements on the sides of the inclusion—dextral on the left side and sinistral on the right side) and with the short (λ_2) axis smaller than the radius of the undeformed circles (implying constriction on the sides of the inclusion). (2) Originally orthogonal straight lines have become curved at the upper rear tail, and between the confining sidewalls and the inclusion (implying differential displacement at the sides of the inclusion). (3) The orientation of the λ_1 axis of strain ellipses changes gradually from normal to the shear direction at the upper rear tail to almost parallel to the shear direction between the inclusion and the sidewalls. (4) The grid on top of the upper front tail has suffered almost no deformation. (5) Deformation of the grid close to the confining sidewalls shows that drag effects are insignificant.

Model 3—two prolate rigid inclusions

The two prolate plasticine inclusions have been moulded with identical principal dimensions $x = 80$ mm and $y = z = 25$ mm, and placed side-by-side on the middle of the top of the lower brown silicone half-layer, with the longest axes coincident with the shear direction. The entire model was subjected to bulk homogeneous simple shear deformation with values of strain rate of about $6.6 \times 10^{-3} \text{ s}^{-1}$ and shear strain close to 7. Knowing the structures developed around one prolate inclusion, our aim with this model has been to try to unravel the interference structures that could develop in the region between the two inclusions. Theoretically, we could expect a sheath fold to develop between the two inclusions as a result of three-dimensional differential flow (Fig. 9). In order to evaluate what would happen between the two inclusions, they should remain side-by-side throughout the experiment. In fact this has not happened in any of the experiments. It has proved practically impossible to make the inclusions of exactly the same density, and so the inclusions settle at different heights in the model. As a result, there is differential displacement between the inclusions and transcurrent movements occur between them. Note that if the rigid inclusion settles at middle height in the model, it will remain stationary relative to an external reference frame because the upper and lower confining plates move at the same velocity. Thus, any deviation from this ideal position will result in a displacement of the inclusion relative to an external reference frame (e.g. if during top-to-right shearing the inclusion settles above middle height of the model, then it will move to the right, and if below it will move to the left). This could be an explanation for the asymmetry of the structures developed around rigid inclusions during the experiments. Folds in

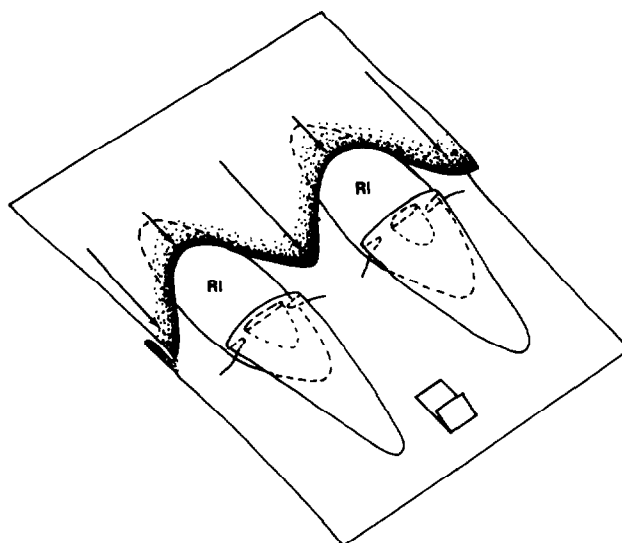


Fig. 9. Predicted fold pattern associated with two inclusions. Rigid inclusions (RI) work as an obstacle to the flow of the matrix and, although the deformation mechanism is bulk layer parallel simple shear, they induce local three-dimensional differential flow close to the upper rear (and symmetrically lower front) parts of the two inclusions. Size of the arrows represent differential displacement.

symmetrical positions around the inclusion usually do not show identical development (see for instance Figs. 4d and 5b).

In one experiment of each model, we used lubricant (neutral liquid soap) around the rigid inclusion and between the two brown silicone half-layers to create greater rheological contrast between inclusion and matrix. The aim was to simulate the high rheological contrast between the boudins of granulate (with recrystallization tails) and surrounding carbonate matrix, as found in some natural shear zones of the Bragança CAT. The result was a greater amplification of the structures obtained without lubricant, especially of the rim folds developed close to the upper rear and lower front parts of the inclusion.

DISCUSSION AND INTERPRETATION OF THE RESULTS

Strain rate

Taking into account that the experiments have been performed at constant volume, variations in the strain rate are expected to occur in the vicinity of the rigid inclusion because: (1) the YZ section of the silicone vertically from the inclusion is smaller than elsewhere in the model (shaded, Fig. 10) and the volume of material existing away from the inclusion (in the upper part of the rear tail and in the lower part of the front tail) must go through that smaller section; (2) the overall strain rate has been kept constant. Keeping in mind that the applied strain rate is constant, particles flowing towards the inclusion must begin to accelerate (differentially

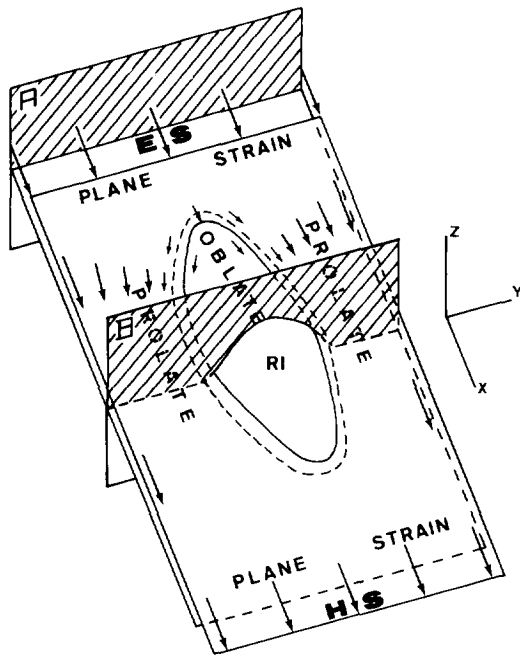


Fig. 10. Sketch of the inferred basic (and thus partial) strain field pattern around a rigid inclusion (RI). Only the upper half of the model is represented. If located in the middle of the model, the inclusion will remain stationary (even in relation to an external reference frame). Thus, planes other than the equatorial (ES) will move and encounter an immobile inclusion that will be an obstacle to the flow of the ductile matrix. The area of section B is smaller than the area of section A and, thus, flowing particles will jam at the upper rear (and symmetrically at the lower front) of the inclusion and will follow complex paths around it. Moreover, sidewalls and inclusion confine the flow of particles in the XY plane. With decrease in the Y and Z directions and increase in the X direction, prolate ellipsoids should develop at this site. Flowing particles will also concentrate at the top of the inclusion; with decrease in the Z direction and increase in the Y and X directions, oblate ellipsoids should develop at this site. Size of arrows indicate differential displacement. Identical arrows away from the rigid inclusion represent uniform displacement. HS—higher surface.

because of non-cylindricity of the inclusion surface) when they reach the YZ section tangent to the apex of the inclusion, attain a maximum at the yz principal section of the inclusion, and from there on return to the overall applied strain rate. Exact patterns of strain rate variations are impossible to measure, or even describe, from our experiments.

Flow and stress field patterns

Because the volume of material away from the inclusion (in the upper part of the rear tail and in the lower part of the front tail) must flow along the non-cylindrical surface of the inclusion and through a smaller section (Fig. 10), flow lines and stress trajectories must follow complex paths in the vicinity of the rigid inclusion. Ductile silicone matrix flowing in the upper rear and lower front parts of the rigid inclusion is subjected to differential compression until it reaches the yz principal section of the inclusion. From there onwards the silicone matrix is subjected to differential extension until it reaches the YZ section of the model tangent to the apex of the inclusion.

Strain pattern

During the experiments we have not kept track of the flow lines and of the three-dimensional strain pattern, but can predict that variations in the shape of the finite strain ellipsoid must take place due to the existence of a rigid body leading to variations in the flow and stress field patterns. We predict that prolate ellipsoids will occur in the lateral zones of the inclusion (Fig. 10) because flow lines must accumulate in the XY section of the model (the areas of the YZ and XY sections of the model are smaller in terms of silicone matrix) and, therefore, the λ_2 axis of the finite strain ellipsoid must decrease. Moreover, from the concurrent effect of simple shear and lateral constriction (exerted by inclusion surface and confining sidewalls) it can be predicted that the λ_1 axis of the finite strain ellipsoid must increase greatly and the λ_2 axis decrease. The dimension of the λ_3 axis of the strain ellipsoid will depend on the joint effects of simple shear and constriction. If simple shear prevails over lateral constriction (as we believe to be the case in view of the value of the applied shear strain), the λ_3 axis of the finite strain ellipsoid becomes gradually smaller than the radius of the initial unit sphere, and a highly prolate ellipsoid develops. As can be seen from Fig. 5(c), predictions for the λ_1 and λ_2 axes of the finite strain ellipsoid seem to be correct. The dimension of the λ_2 axis of the finite strain ellipsoids, in the zones between the inclusion and the confining sidewalls, is much smaller, and the dimension of the λ_1 axis much greater, than the radius of the initial undeformed circle.

Oblate ellipsoids should occur associated with the uppermost and lowermost regions of the rigid object, where flow lines must accumulate in the XZ section and where simple shear and vertical constriction are concurrent to make the λ_3 axis of the finite strain ellipsoid decrease and the λ_2 axis increase.

Plane strain ellipsoids should occur away from the field of influence of the inclusion (where the deformation regime is homogeneous simple shear) and at the sites of transition between the prolate and oblate ellipsoids. When populations of inclusions are considered, more complex strain and flow field patterns can be expected. We believe that the main feature is the most probable occurrence of prolate ellipsoids between two inclusions, as the result of constriction in a situation similar to that of an inclusion and a confining sidewall.

Deformation regime

Although the applied deformation regime was bulk homogeneous simple shear, significant heterogeneities were induced by the presence of a rigid body, so other deformation regimes must operate locally in its vicinity.

The sheath folds formed at the upper front and lower rear parts of the rigid inclusions have developed in a similar fashion to model 2 of Cobbold & Quinquis (1980): passive folding resulting from simple shearing of a non-cylindrical surface. The difference is that the surface of the competent layer is here not concave

upwards (as in model 2 of Cobbold & Quinquis 1980), but convex up and downwards (bi-convex).

The strongly non-cylindrical rim folds formed at the lower front and upper rear have developed by a combination of three-dimensional differential flow and simple shear. Three-dimensional differential flow results from the fact that the flowing silicone matrix encounters a rigid non-cylindrical surface that works as an obstacle to the flow of the silicone. Thus, ductile matrix trying to flow at the lower front and upper rear of the rigid inclusion accumulates and enters the contraction field. From early in the experiment, the inclusion rotates antithetically, i.e. anticlockwise during top-to-the-right shear. This rotation induces deformation (deflection) in the surrounding ductile matrix and the result is the development of a non-cylindrical surface around the lower front and upper rear of the inclusion. This surface acted on simultaneously by simple shear and three-dimensional flow develops into a strongly non-cylindrical fold (rim fold).

Inclusion behaviour and kinematic indicators

Ghosh & Ramberg (1976) theoretically investigated the reorientation of rigid ellipsoidal particles immersed in a viscous medium during a combination of simultaneous pure and simple shear, and showed that the inclusion may rotate backwards, depending on the axial ratio of the ellipsoidal particle ($R = x/z$) and on the ratio of pure shear to simple shear (S_p). According to Ghosh & Ramberg (1976, fig. 43), particles should rotate forward indefinitely if S_p is zero (i.e. if the only component is simple shear), independently of the axial ratio of the rigid ellipsoidal particle. Moreover, these authors showed that there are two critical orientations (one stable and one metastable) at which the rate of rotation becomes zero. The orientation at which rotating inclusions ultimately come to a stable position is always inclined towards the top shear sense and, in the limiting case, becomes parallel to the shear plane. In all their theoretical development, Ghosh & Ramberg (1976) do not account for the finite width of the shear zone, which we believe to be an important and key factor. Jeffery (1922) and Ghosh & Ramberg (1976) considered the inclusion embedded in an infinite matrix, which is not the case in our experiments. The dimension of the immersed rigid inclusion is relatively large compared with the finite width of our models.

Taking into account (i) the axial ratios of the rigid ellipsoidal inclusions used in our experiments ($2.2 < R < 3.4$), (ii) the initial position of the ellipsoidal particle with its xy plane parallel to the shear plane, (iii) the fact that the applied bulk strain was simple shear, and (iv) the theoretical predictions of Ghosh & Ramberg (1976), we should expect the inclusions to rotate continuously during our experiments because S_p is supposedly equal to zero. However, in most of our experiments, the rigid inclusion has early tilted backwards and kept this position throughout the experiment; i.e. the equatorial plane of the inclusion has rotated antithetically to the

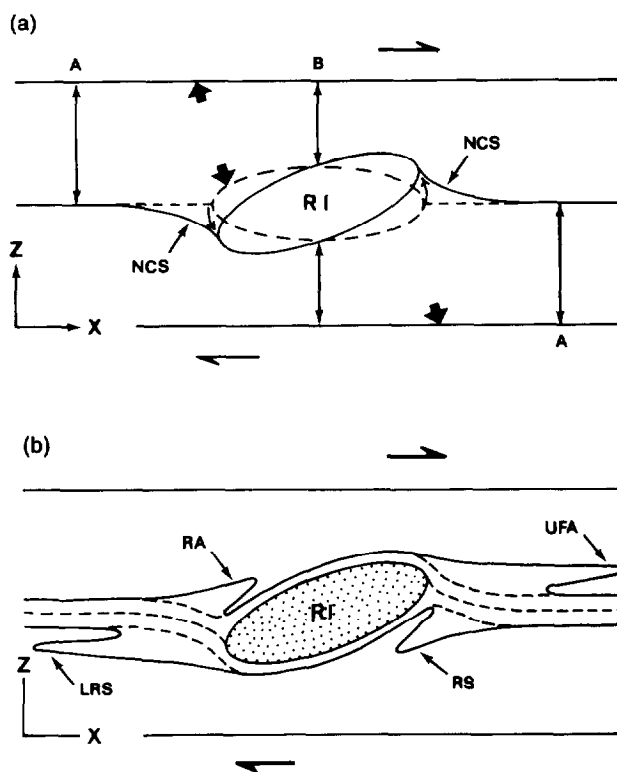


Fig. 11. Sketch to illustrate rotation of the rigid inclusion (RI) and subsequent development of rim folds. (a) As soon as shear starts, silicone is compressed when it reaches the upper rear and lower front of the competent inclusion (because the section in B is smaller than the section in A) and react by pushing it (thick arrows). This rotation of the inclusion produces a non-cylindrical surface (NCS) that is folded in the continuation of motion, giving rise to the rim anticlines (RA) and synclines (RS) illustrated in (b). (b) Complete fold pattern developed around the competent inclusion: upper frontal anticlinal (UFA) and lower rear synclinal (LRS) sheath folds develop from the non-cylindrical surface of the brown silicone layers wrapping around the inclusion; rim anticlines and synclines develop because of local three-dimensional differential flow and from the non-cylindrical surface resulting from rotation of the inclusion. In (a) only the interface between the two brown silicone half-layers is represented. Dashed lines represent initial positions.

applied sense of shear and has stabilized inclined opposite to the top sense of shear. We believe that the most logical explanation can be found in the size relation between rigid ellipsoidal inclusion (in particular its z dimension) and the width of shear zone (in our experiments the spacing between top and bottom walls of the simple shear machine). If the inclusion is big enough to reduce significantly the section through which the silicone matrix must pass, then the deformation regime is no longer only simple shear in the influence field of the inclusion. As soon as shear starts, the particles in motion begin to jam and exert pressure at the upper rear and lower front parts of the rigid inclusion and these will thus be pulled respectively down and upwards as a result of the induced compression (see XZ section in Fig. 11). Symmetrically, the upper front and lower rear parts will be pushed respectively up and down because of tension exerted by the moving top and bottom plates and as a result of movement of silicone matrix in the opposite quadrants.

This geometry is identical to that observed in the natural example illustrated in Fig. 4(c), a σ tailed bou-

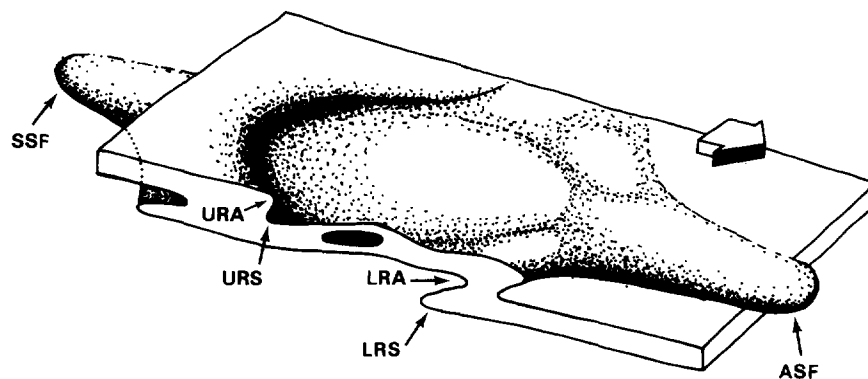


Fig. 12. Complete pattern of folds around a rigid inclusion. Reconstruction based on results of all experiments, especially on the results obtained with transparent silicone. ASF—upper frontal anticlinal sheath fold. LRA—lower frontal rim anticline. LRS—lower frontal rim syncline. SSF—lower rear synclinal sheath fold. URS—upper rear rim syncline. URA—upper rear rim anticline.

din. This phenomenon may be the result of the size relation between the boudin and the thickness of the shear zone or the spacing of C surfaces (shear band foliation). If boudins (or rigid inclusions) are big enough compared with finite shear zone thickness or shear band spacing, then considerable problems of space will arise and the matrix flowing between ductile shear zone walls (Fig. 11), or between C surfaces, will have to follow complex paths between inclusions and will exert differential pressure at different sites of the inclusions. In the case of C surfaces, these would work as walls of microscopic shear zones. This may be the case of type-II S - C mylonites of Lister & Snoke (1984) and σ_b porphyroclasts of Passchier & Simpson (1986). In Fig. 3(c) we present an example of a typical σ porphyroclast system in gneisses from the Bragança complex. The central porphyroclast is clearly dipping to the right (although sense of shear is top to the left) and is bounded, both below and above, by shear bands (C surfaces) marked by the concentration of finely recrystallized mica (darker traces on the image). This tilting opposite to the top shear sense (backward tilting) is a common geometric feature in the Bragança complex, rather than sporadic, which seems to indicate that this is a stable position. In most cases (if not all), as in Figs. 3(c) and 4(c), we do not observe any traces of synthetical rotation of the porphyroclast. Thus, we suggest that these porphyroclasts were originally parallel to the shear plane and that they have rotated antithetically. A possible explanation for this back-rotation is the size relationship between spacing of C surfaces and porphyroclast, because this rigid inclusion considerably reduces the section through which the ductile, finely recrystallized matrix must pass, as has happened with the rigid inclusions in our experiments. Another explanation for the possible antithetical rotation of porphyroclasts has been provided by Ildefonse & Mancktelow (1993) when slip occurs along the matrix/clast interface.

Simpson & De Paor (1993) refer to the co-existence of σ and δ porphyroclast systems in the same outcrop, or even on the same flow plane, which is a feature not uncommon in the region of the Bragança Massif. The

explanation Simpson & De Paor (1993) provide is "... to start with grains of very different axial ratio and/or orientation". This explanation seems correct and complete, provided that σ grains are not systematically tilted backwards. Otherwise, another explanation is required because, as theoretically shown by Ghosh & Ramberg (1976), even during a combination of simultaneous pure and simple shear the rigid inclusion may rotate antithetically, with the limit parallel to the shear plane, but never past (or beyond) the shear plane, i.e. tilted backwards. Then, if σ porphyroclasts are systematically tilted backwards, this may be the result of a narrow ductile shear zone compared with porphyroclast dimensions. To conclude, the co-existence of σ (tilted backwards) and δ grains in the same flow plane may result from the combined effect of initial axial ratio and/or orientation of the grains, and/or size relationship between grains and finite shear zone width, and/or slip on the matrix/clast interface (Ildefonse & Mancktelow 1993).

If the rigid inclusions in our experiments were more equidimensional, or elongated normal to the shear direction (parallel to the Y -axis), they would most probably rotate continuous and synthetically with the applied sense of shear as theoretically predicted by Ghosh & Ramberg (1976).

In many natural cases, boudins exhibit symmetrical tails, thus being impossible to deduce the shear sense from them. Symmetrical tails may be the consequence of post-kinematic recrystallization and reequilibration due to overburden (e.g. Mawer 1987), or due to slip on the interface (Ildefonse & Mancktelow 1993) between highly competent HP/HT granulite and highly ductile carbonate matrix, or the result of a particular relationship between S , and R (Ghosh & Ramberg 1976). But if the boudin has associated folds, then it may be possible to deduce the shear sense from the fold pattern (Figs. 4d, 5b and 12). Z-shaped folds all around a competent inclusion indicate top to the right (or dextral) sense of shear, and S-shaped folds all around a competent inclusion indicate top to the left (or sinistral) sense of shear. When encountered around natural rigid inclusions, such fold patterns may provide useful indi-

cators of the deformation regime. It is difficult to envisage a regime either than bulk simple shear that could be responsible for such a pattern.

CONCLUSIONS

The presence of a rigid body (relatively large) embedded in a ductile matrix (relatively thin) induces complex strain and flow field patterns on its vicinity (influence field). Finite strain ellipsoids vary from prolate to oblate around the rigid inclusion and away from it.

Competent inclusions work as an obstacle to the flow of the matrix, thus generating local three-dimensional differential flow associated with layer parallel bulk simple shear.

The sheath folds formed at the upper front and lower rear parts of the rigid inclusions presumably developed in a similar fashion to model 2 of Cobbold & Quinquis (1980). The highly non-cylindrical folds formed at the lower front and upper rear must have developed by a combination of simple shear and three-dimensional differential flow.

In our experiments, both prolate (with longest axis parallel to the shear direction) and oblate inclusions have rotated antithetically with respect to bulk shear, early, and remained tilted backwards throughout the experiments. This seems to be the result of differential pressure exerted symmetrically on different parts of the inclusion. Differential pressure results from a particular ratio between finite shear zone width and dimension of the inclusion.

Sense of shear is consistent all around the rigid inclusion and consistent with applied bulk sense of shear. The fold pattern developed around rigid boudins may be used as a shear sense criterion.

In natural shear zones, the fold patterns around rigid boudins is more complex than those observed in the experiments, because (1) populations of smaller boudins gather, and flowing ductile matrix jams, in the upper rear and lower front parts of the boudin, and (2) active folds result from rheological contrasts in the foliation and metamorphic layering.

If rigid inclusions are of cartographic scale (e.g. mafic/ultramafic intrusions as in the case of the Bragança examples, then variations in the strain pattern should also be expected to occur at the macroscopic scale during bulk simple shear deformation.

Acknowledgements—Experiments were carried out in the Laboratoire de Tectonophysique in the University of Rennes, France. F. Marques acknowledges a INIC/JNICT doctoral scholarship. Field work carried out by F. Marques was partly supported by EEC project MA1M-0075-C (TT) and by TESIS research programme (PMCT/C/CEN/102/90).

REFERENCES

- Bretherton, F. P. 1962. The motion of rigid particles in a shear flow at low Reynolds number. *J. Fluid Mech.* **14**, 284–304.
- Brun, J.-P. & Merle, O. 1988. Experiments on folding in spreading-gliding nappes. *Tectonophysics* **145**, 129–139.
- Cobbold, P. R. & Quinquis, H. 1980. Development of sheath folds in shear regimes. *J. Struct. Geol.* **2**, 119–126.
- Cox, R. G. 1971. The motion of long slender bodies in a viscous fluid. 2—shear flow. *J. Fluid Mech.* **45**, 625–657.
- Donath, F. A. & Parker, R. B. 1964. Folds and folding. *Bull. geol. Soc. Am.* **75**, 45–62.
- Ferguson, C. C. 1979. Rotations of elongate rigid particles in slow non-Newtonian flows. *Tectonophysics* **60**, 247–262.
- Freeman, B. 1985. The motion of rigid ellipsoidal particles in slow flows. *Tectonophysics* **113**, 163–183.
- Gay, N. C. 1968. The motion of rigid particles embedded in a viscous fluid during pure shear deformation of the fluid. *Tectonophysics* **5**, 81–88.
- Ghosh, S. K. 1975. Distortion of planar structures around rigid spherical bodies. *Tectonophysics* **28**, 185–208.
- Ghosh, S. K. & Ramberg, H. 1976. Reorientation of inclusions by combination of pure shear and simple shear. *Tectonophysics* **34**, 1–70.
- Ghosh, S. K. & Sengupta, S. 1973. Compression and simple shear of test models with rigid and deformable inclusions. *Tectonophysics* **17**, 133–175.
- Ghosh, S. K. & Sengupta, S. 1984. Successive development of plane noncylindrical folds in progressive deformation. *J. Struct. Geol.* **6**, 703–709.
- Harris, J. B., Nawaz, M. & Pittman, J. F. T. 1979. Low-Reynolds-number motion of particles with two or three perpendicular planes of symmetry. *J. Fluid Mech.* **95**, 415–429.
- Hinch, E. J. & Leal, L. G. 1979. Rotation of small non-axisymmetric particles in a simple shear flow. *J. Fluid Mech.* **92**, 591–608.
- Ildefonse, B. & Mancktelow, N. S. 1993. Deformation around rigid particles: the influence of slip at the particle/matrix interface. *Tectonophysics* **221**, 345–359.
- Ildefonse, B., Sokoutis, D. & Mancktelow, N. S. 1992. Mechanical interactions between rigid particles in a deforming ductile matrix. Analogue experiments in simple shear flow. *J. Struct. Geol.* **14**, 1253–1266.
- Jeffery, G. B. 1922. The motion of ellipsoidal particles immersed in a viscous fluid. *Proc. R. Soc. Lond. Ser. A* **102**, 161–179.
- Lister, G. S. & Snoko, A. W. 1984. S–C mylonites. *J. Struct. Geol.* **6**, 617–638.
- Marques, F. G. 1989. Estudo estrutural das rochas catazonais do sinforma de V. Boa de Ousilhão (Bragança, Trás-os-Montes, NE Portugal). Unpublished M.Sc. Thesis, Faculty of Sciences, University of Lisbon.
- Marques, F. G. 1993. Estudo tectónico das rochas infracrustais do manto de soco do SW do Maciço de Bragança (Trás-os-Montes, NE Portugal). Unpublished Ph.D. Thesis, Faculty of Sciences, University of Lisbon.
- Marques, F. G., Ribeiro, A. & Pereira, E. 1992. Tectonic evolution of the deep crust: Variscan reactivation by extension and thrusting of Precambrian basement in the Bragança and Morais Massifs (Trás-os-Montes, NE Portugal). *Geod. Acta* **5**, 135–151.
- Mason, S. G. & Manley, R. St. J. 1957. Particle motion in sheared suspension: orientations and interactions of rigid rods. *Proc. R. Soc. Lond. Ser. A* **238**, 117–131.
- Mawer, C. K. 1987. Shear criteria in the Grenville Province, Ontario, Canada. *J. Struct. Geol.* **9**, 531–539.
- Munhá, J. M. & Marques, F. G. 1987. A model for the lower continental crust (Morais and Bragança Massifs, NE Portugal): II. Petrology. *Terra Cognita* **7**(2/3), 161.
- Munhá, J. M. & Marques, F. G. 1988. Evolução metamórfica das rochas granulíticas no Maciço de Bragança (NE Portugal). *Y Reunión sobre a Geologia do Oeste Peninsular* (abstract volume), Bragança.
- Passchier, C. W. & Simpson, C. 1986. Porphyroclast systems as kinematic indicators. *J. Struct. Geol.* **8**, 831–843.
- Passchier, C. W. & Sokoutis, D. 1993. Experimental modelling of mantled porphyroclasts. *J. Struct. Geol.* **15**, 895–909.
- Reed, L. J. & Tryggvason, E. 1974. Preferred orientations of rigid particles in a viscous matrix deformed by pure shear and simple shear. *Tectonophysics* **24**, 85–98.
- Simpson, C. & De Paor, D. G. 1993. Strain and kinematic analysis in general shear zones. *J. Struct. Geol.* **15**, 1–20.
- Skjernaa, L. 1989. Tubular folds and sheath folds: definitions and conceptual models for their development, with examples from the Grapesvare area, northern Sweden. *J. Struct. Geol.* **11**, 689–703.
- Taylor, G. I. 1923. The motion of ellipsoidal particles in a viscous fluid. *Proc. R. Soc. Lond. Ser. A* **103**, 58–61.

- Van den Driessche, J. 1986. Structures d'enroulement et sens de cisaillement. *C. R. Acad. Sci., Paris* **303**, 413–418.
- Van den Driessche, J. & Brun, J.-P. 1987. Rolling structures at large shear strain. *J. Struct. Geol.* **9**, 691–704.
- Weijermars, R. 1986a. Flow behaviour and physical chemistry of bouncing putties and related polymers in view of tectonic laboratory applications. *Tectonophysics* **124**, 325–358.
- Weijermars, R. 1986b. Polydimethyloxane flow defined for experiments in fluid dynamics. *Appl. Phys. Lett.* **48**, 109–111.
- Weijermars, R. 1986c. Finite strain of laminar flows can be visualized in SGM 36-polymer. *Naturwissenschaften* **73**, 33.